QUANTUM PHYSICS

10.1126/sciadv.1501015

Quantum entanglement at ambient conditions in a macroscopic solid-state spin ensemble

Paul V. Klimov,[1,2] Abram L. Falk,[1,3] David J. Christle,[1,2] Viatcheslav V. Dobrovitski,[4] David D. Awschalom[1]*

Entanglement is a key resource for quantum computers, quantum-communication networks, and high-precision sensors. Macroscopic spin ensembles have been historically important in the development of quantum algorithms for these prospective technologies and remain strong candidates for implementing them today. This strength derives from their long-lived quantum coherence, strong signal, and ability to couple collectively to external degrees of freedom. Nonetheless, preparing ensembles of genuinely entangled spin states has required high magnetic fields and cryogenic temperatures or photochemical reactions. We demonstrate that entanglement can be realized in solid-state spin ensembles at ambient conditions. We use hybrid registers comprising of electron-nuclear spin pairs that are localized at color-center defects in a commercial SiC wafer. We optically initialize 10^3 identical registers in a 40-μm^3 volume (with $0.95^{+0.05}_{-0.07}$ fidelity) and deterministically prepare them into the maximally entangled Bell states (with 0.88 ± 0.07 fidelity). To verify entanglement, we develop a register-specific quantum-state tomography protocol. The entanglement of a macroscopic solid-state spin ensemble at ambient conditions represents an important step toward practical quantum technology.

INTRODUCTION

Nuclear spin ensembles in room-temperature liquids were among the first platforms to be explored for executing quantum algorithms (*1*–*3*). In these systems, nuclear spins encode the quantum computational bits (qubits) (*4*), and nuclear magnetic resonance pulses are used to perform quantum-logic operations. The small nuclear magnetic moment, which gives nuclei their long-lived spin coherence, also prevents them from reaching a large thermal polarization (<10% of ^{29}Si are polarized at 25 mK in a 10-T magnetic field). This has largely constrained quantum algorithms to be executed on weakly initialized pseudo-pure states (*5*) of nuclear spins, which cannot be genuinely entangled (*6*).

A way to overcome the limitations of weakly initialized states is to encode qubits in collections of interacting nuclear and electron spins. Such hybrid systems (*7*–*17*) combine the long-lived nuclear spin coherence with the electron's ability to interact relatively strongly with magnetic and optical fields. These latter features facilitate the strong initialization of hybrid systems via the cryogenic or optical polarization of their electron spins followed by polarization transfer to their nuclear spins. In recent years, the cryogenic cooling approach has led to low-temperature, high–magnetic field ensemble entanglement in Si (*7*), showing promise for hybrid spin architectures.

A longstanding challenge has been to realize entanglement in a macroscopic spin ensemble at ambient conditions. Overcoming this challenge would represent a key step toward quantum technologies for several reasons: First, ensembles comprising N spins benefit from the $N^{1/2}$ scaling of both their spin signal-to-noise ratio and their coupling strength to external degrees of freedom (*18*–*23*). Second, entangled spins are compatible with a broad range of quantum information processing techniques such as quantum error correction (*24*, *25*), which could be used to mitigate decoherence and rethermalization. Finally, cryogen-free and low–magnetic field functionality would facilitate the development of practical quantum devices.

Hybrid systems based on color-center defects in semiconductors (*8*–*17*, *26*–*36*) are ideal platforms for realizing quantum phenomena at ambient conditions because they have atom-like states that exhibit both room-temperature spin coherence and spin polarization through optical pumping. Indeed, entanglement has been studied in single nitrogen-vacancy color centers in diamond (*11*–*15*). However, because of challenges that include addressing specific hybrid systems embedded within a complex ensemble, realizing entanglement in a spin ensemble at ambient conditions has remained an open problem.

We develop a general methodology for solving this problem, using PL6 color centers (*16*, *17*, *28*, *30*, *33*) in 4*H*-SiC for our demonstration. PL6 color centers localize electronic states that are characterized by a near–telecom wavelength optical transition and a ground-state spin (S = 1) with gigahertz frequency addressability. This spin couples to the nuclear spin of ^{29}Si (I = ½, 4.7% natural abundance) and ^{13}C (I = ½, 1.1% natural abundance) isotopic defects via the hyperfine interaction. In configurations where a nuclear spin resides within several lattice sites of PL6, the hyperfine interaction exceeds both the electron and nuclear spin dephasing rates and thus strongly couples the two-spin system. In our samples, the most abundant strongly coupled systems comprise single PL6 electron spins and single ^{29}Si nuclear spins (see Fig. 1A, Materials and Methods, and section S1 for details). Such spin pairs serve as two-qubit hybrid registers with an electron-spin qubit that is encoded by the m_S = 0 and m_S = −1 spin states and a nuclear-spin qubit encoded by the $m_I = \downarrow$ and $m_I = \uparrow$ spin states (Fig. 1B). Here, we show that an ensemble of identical registers can be prepared into the maximally entangled Bell states (Fig. 1C) at ambient conditions. To generate and verify this entanglement, we combine register initialization and readout, quantum-logic gates, and quantum-state tomography.

RESULTS

To initialize registers, we use the PL6 spin-dependent optical cycle. Electrons localized at PL6 defects can be optically pumped into their m_S = 0 spin sublevels with nonresonant laser light, through an electron spin–dependent intersystem-crossing pathway. We determine the

[1]Institute for Molecular Engineering, University of Chicago, Chicago, IL 60637, USA. [2]Department of Physics, University of California, Santa Barbara, CA 93106, USA. [3]IBM T. J. Watson Research Center, 1101 Kitchawan Road, Yorktown Heights, NY 10598, USA. [4]Ames Laboratory and Iowa State University, Ames, IA 50011, USA.
*Corresponding author. E-mail: awsch@uchicago.edu

degree of electron spin polarization to be 93^{+7}_{-11}% through a spin-resolved measurement of the PL6 optical cycle (see section S2 for details). ^{29}Si nuclei that are strongly coupled to PL6 electrons can be optically polarized into their $m_I = \uparrow$ states through dynamic nuclear polarization, which is strongest at $B_{||}$ = 33 mT (*16*, *17*). The mechanism responsible for this polarization is a hyperfine-mediated spin exchange, from the electron to the nucleus, in each register's optically excited state. We determine the degree of nuclear spin polarization to be as high as 99^{+1}_{-3}% through the tomography procedure that we later describe. For comparison, under similar conditions, electrons localized at single nitrogen-vacancy centers in diamond can be optically polarized to ~65% (*36*) and strongly coupled nuclei can be dynamically polarized to ~98% (*9*). To obtain a similar thermal nuclear spin polarization, the sample would have to be cooled to 2.5 μK at 33 mT or, equivalently, immersed in a 4-MT magnetic field at 296 K. We use these mechanisms to optically initialize registers into the pure $|m_S, m_I\rangle = |0, \uparrow\rangle$ state with high fidelity at room temperature.

The optical cycle that drives initialization also enables us to independently probe registers' electron and nuclear spin components. In particular, nonradiative processes in the intersystem-crossing pathway lead a register's time-averaged photoluminescence intensity to depend on its electron spin state (*28*). We can therefore probe registers' electron spins by applying a resonant microwave field while monitoring changes to the photoluminescence. This readout method is known as optically detected magnetic resonance (ODMR). Near 33 mT, where an optically excited register's nucleus can exchange spin polarization with its coupled electron (*16*, *17*), we find that the time-averaged photoluminescence intensity also depends on the register's nuclear spin state. We can therefore directly read out the registers' nuclear spins by applying a resonant radio-frequency field while monitoring changes to the photoluminescence [see Steiner *et al.* (*10*) and Materials and Methods]. This readout method is known as optically detected nuclear magnetic resonance (ODNMR).

To characterize the registers' electron spin transition frequencies, we perform ensemble ODMR spectroscopy (Fig. 2A) (*28*). This measurement reveals a strong single resonance—the $|-1\rangle \leftrightarrow |0\rangle$ resonance of PL6 electron spins that are not strongly coupled to any nuclei—and three surrounding doublets (Fig. 2B). The two pronounced doublets (blue and purple traces) are the hyperfine-split electron spin resonances, $|-1, \downarrow\rangle \leftrightarrow |0, \downarrow\rangle$ and $|-1, \uparrow\rangle \leftrightarrow |0, \uparrow\rangle$, of two distinct registers, which we label R1 and R2. R1 and R2 differ in that their respective ^{29}Si nuclear spins occupy inequivalent lattice sites relative to the PL6 defect (*16*). The third doublet (green trace), which we believe results from registers comprising single PL6 electron spins and single ^{13}C nuclear spins (*16*), was not considered because of its weak signal. In our optical interrogation volume, there are about 10^3 R1 and R2 registers (see section S3).

To characterize the registers' nuclear spin transition frequencies, we perform ODNMR spectroscopy (Fig. 2C) (*12*). This measurement reveals two resonances, which are the $|-1, \downarrow\rangle \leftrightarrow |-1, \uparrow\rangle$ hyperfine transitions of R1 and R2 (Fig. 2D). Both resonances evolve with magnetic field according to the ^{29}Si gyromagnetic ratio, confirming that the nuclei in R1 and R2 are ^{29}Si (Fig. 2D, inset; see Materials and Methods for details). Because of the long nuclear spin coherence, the registers' ODNMR resonances are much narrower than their ODMR counterparts. This fact enables our entangling algorithm and motivates the use of nuclear spins for quantum memory. Moreover, because the resonances are spectrally isolated, we can selectively address the R1 or R2 ensemble through ODNMR with virtually no crosstalk (see section S4 for nuclear Rabi, Ramsey, and Hahn-echo measurements).

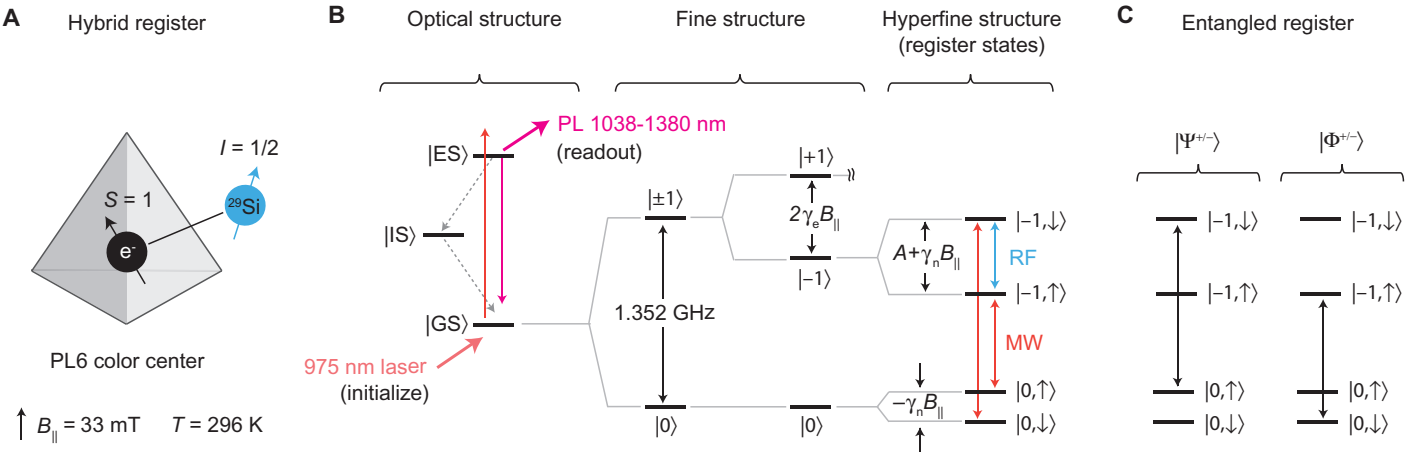

Fig. 1. Hybrid registers in silicon carbide. (**A**) A hybrid two-qubit register comprising a PL6 color-center defect's intrinsic electron spin and a nearby ^{29}Si nuclear spin. The PL6 defect, whose physical structure is unknown, is depicted as a pyramid to indicate its known C_{3v} symmetry. (**B**) The hybrid system forms an atom-like state with an optical, fine, and hyperfine structure. Optical pumping from the ground state $|GS\rangle$ to the excited state $|ES\rangle$ with nonresonant laser light initializes registers into $|0, \uparrow\rangle$. The mechanisms responsible for initialization are a series of electron spin–dependent intersystem crossings (dashed arrows), through some intermediate states $|IS\rangle$, and dynamic nuclear polarization. These mechanisms also lead the intensity of the emitted photoluminescence to be dependent on both the electron and nuclear spin, enabling registers to be read out. The energy levels are split by the crystal field, the electron and nuclear Zeeman effects ($2\gamma_e B_{||}$ and $-\gamma_n B_{||}$, where γ_e = 28 MHz/T, γ_n = −8.5 MHz/T for ^{29}Si, and $B_{||}$ is a magnetic field co-aligned with the PL6 symmetry axis), and the hyperfine interaction (A). The register states are $|-1, \uparrow\rangle$, $|0, \downarrow\rangle$, $|-1, \downarrow\rangle$, and $|0, \uparrow\rangle$. Radio-frequency (RF) and microwave (MW) pulses are used to drive nuclear and electron spin transitions, respectively. (**C**) A register's electron and nuclear spin can be entangled by using MW and RF pulses to produce coherences (indicated by double-ended arrows) between the $|-1, \uparrow\rangle$ and $|0, \downarrow\rangle$ states or between the $|-1, \downarrow\rangle$ and $|0, \uparrow\rangle$ states. We prepare 10^3 identical registers into each of the four Bell states, $|\Psi^{\pm}\rangle$ and $|\Phi^{\pm}\rangle$.

Having characterized the electron and nuclear spin transition frequencies of R1 and R2, we develop quantum gates for their systematic control within the circuit model of quantum information processing. Local gates, which operate on one spin of a given register irrespective of the state of the other spin in that register, are implemented with broadband frequency pulses (for example, the electronic NOT_e gate, which drives $|0,\downarrow\rangle \leftrightarrows |-1,\downarrow\rangle$ and $|0,\uparrow\rangle \leftrightarrows |-1,\uparrow\rangle$). Nonlocal gates, whose operation on one spin of a given register is conditional on the state of the other spin in that register, are implemented with narrowband frequency pulses (for example, the electronic $C_{\downarrow}NOT_e$ gate, which drives $|0,\downarrow\rangle \leftrightarrows |-1,\downarrow\rangle$, while leaving the populations in $|0,\uparrow\rangle$ and $|-1,\uparrow\rangle$ unperturbed). For universal control (*4*) over R1 and R2, we calibrate the electronic nonlocal $C_{\downarrow}ROT_e$, $C_{\uparrow}ROT_e$, and local ROT_e gates as well as the nuclear nonlocal $C_{-1}ROT_n$ gate. ROT indicates a spin rotation, which we can apply with arbitrary angle θ and phase ϕ (see Fig. 3A).

Using calibrated quantum gates, we develop a method to selectively reconstruct the density matrix (ρ) of the R1 or R2 ensemble via quantum-state tomography. In our method, we iteratively prepare a register ensemble into its to-be-measured quantum state and then project its coherences (off-diagonal ρ elements) and populations (on-diagonal ρ elements) onto those registers' ODNMR resonance for readout. The quantum circuits used for these measurements, which were designed to mitigate readout errors, are presented in Fig. 3 (B to D). Because unitary operations can only probe population differences between spin states, these circuits resolve the elements of ρ up to a normalization factor. We determine this factor from the independent measurement of the optically pumped electron spin polarization mentioned earlier. By extracting the elements of ρ from a well-isolated ODNMR resonance (Fig. 2D), as opposed to a spectrally overlapping ODMR resonance (Fig. 2B), we obtain a reconstruction with virtually no parasitic signal from inequivalent registers or other spin systems. This procedure differs from the tomography protocols that have been applied to single color centers (*8*, *11*–*15*), which rely on electron spin readout. The full details of our tomography procedure are given in section S5.

Having established register initialization, readout, quantum gates, and tomography, we have the necessary components to generate and detect entanglement. Our entangling algorithm (Fig. 3E) consists of the following steps: we optically initialize registers into $|0,\uparrow\rangle$ and then evolve them into the state $|-1,\uparrow\rangle$ with a series of nonlocal electronic gates. We then apply a nonlocal nuclear gate to prepare them into the coherent nuclear spin superposition $2^{(-1/2)}(|-1,\uparrow\rangle \pm |-1,\downarrow\rangle)$ and then apply a nonlocal electronic gate to project this coherence into one of the four Bell states

$$|\Psi^{+/-}\rangle = \frac{1}{\sqrt{2}}\left(|0,\uparrow\rangle \pm |-1,\downarrow\rangle\right) \quad (1)$$

$$|\Phi^{+/-}\rangle = \frac{1}{\sqrt{2}}\left(|0,\downarrow\rangle \pm |-1,\uparrow\rangle\right) \quad (2)$$

We execute this algorithm on either the R1 or R2 ensemble and, in separate experimental runs, tomographically reconstruct the initial

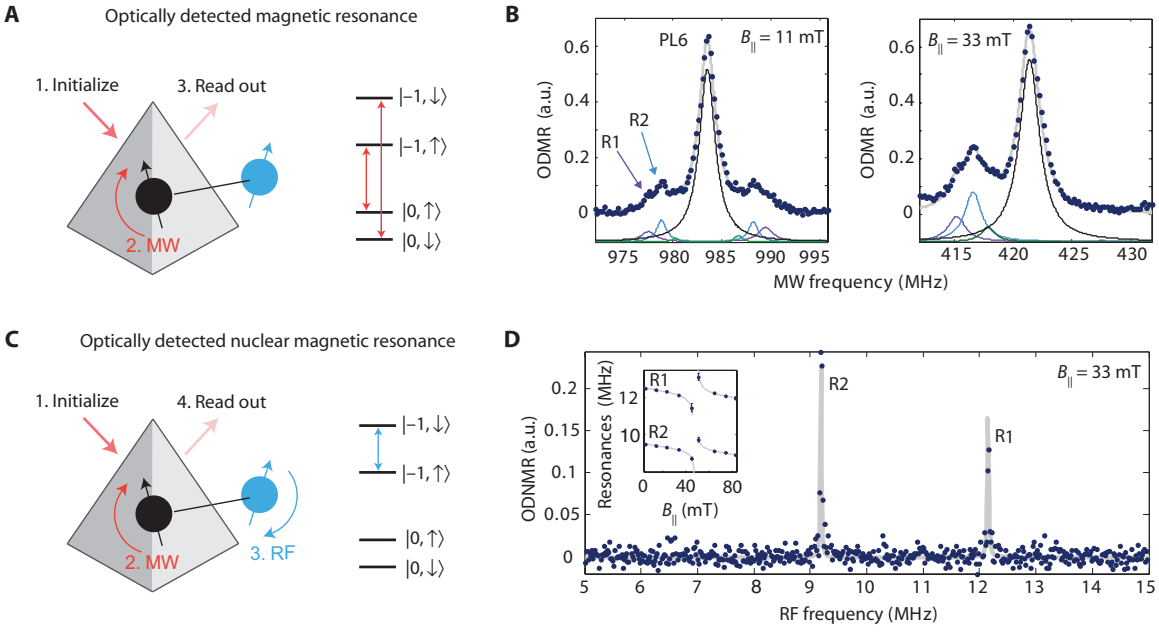

Fig. 2. Register characterization. (**A**) ODMR measurement sequence. (**B**) ODMR returns a structured line that can be decomposed into a strong central resonance and three doublets (the model curves, which are derived from fits to the data, are offset). The central peak (black trace) is the $|0\rangle \leftrightarrow |-1\rangle$ resonance of PL6 electron spins that are not strongly coupled to any nuclei. The two pronounced doublets (blue and purple traces) are the $|0,\uparrow\rangle \leftrightarrow |-1,\uparrow\rangle$ and $|0,\downarrow\rangle \leftrightarrow |-1,\downarrow\rangle$ transitions of two inequivalent types of register (labeled R1 and R2; the arrows are color-coded to the model curves). The third doublet (green trace) was not considered in this study because of its weak signal. (Right) At $B_{||}$ = 33 mT, dynamic nuclear polarization strongly initializes the nuclei in R1 and R2 into their $m_I = \uparrow$ states. This is observed in ODMR as a strong asymmetry in the amplitudes of the individual peaks in each doublet. a.u., arbitrary units. (**C**) ODNMR measurement sequence. (**D**) ODNMR returns two sharp peaks, which are the $|-1,\uparrow\rangle \leftrightarrow |-1,\downarrow\rangle$ resonances of R1 and R2. (Inset) Both resonances evolve with magnetic field according to the ^{29}Si gyromagnetic ratio. ODMR and ODNMR are obtained through differential photoluminescence measurements, which are described in Materials and Methods.

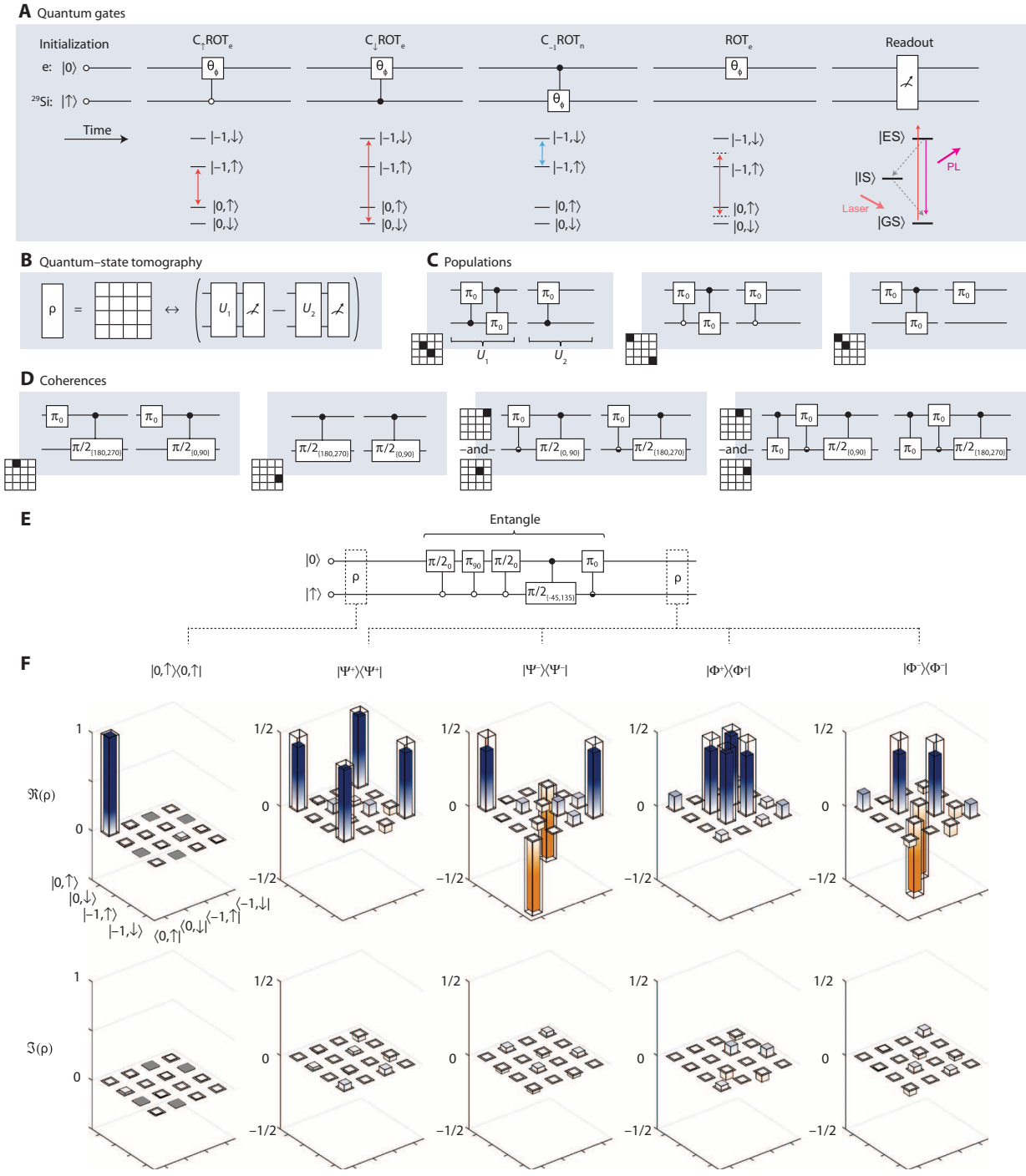

Fig. 3. Register entanglement. (**A**) Quantum gates within the circuit model of quantum information processing and their implementation in our system. Initialization and readout use the same optical cycling process. (**B**) The density matrix ρ is reconstructed by making 15 differential measurements between distinct quantum circuits U_1 and U_2. Each measurement allows us to infer either a single element or a relationship between two elements of ρ. (**C**) The three circuit pairs used to determine the relationships between the four populations. U_1 and U_2 are labeled to serve as a guide for all circuit pairs. (**D**) The 12 circuit pairs used to determine the real and imaginary components of the six unique coherences. We use a condensed notation in which half-filled circles are used to combine circuit pairs that differ in the condition of a gate and brackets to combine those that differ in the phase of a gate. (**E**) Entangling algorithm. The Bell state is chosen by the phase of the last nuclear gate and the condition of the last electronic gate. (**F**) The real (upper panel) and imaginary (lower panel) components of the R2 ensemble density matrix after optical pumping and after the entangling algorithm. The overlaid transparent bars represent the ideal density matrices. The normalization for these reconstructions is derived from the mean electron spin polarization. The coherences $\langle 0,\uparrow|\rho|-1,\uparrow\rangle$ and $\langle 0,\downarrow|\rho|-1,\downarrow\rangle$, which are shown as gray squares in the initial ρ, are not measured in our experiments. See section S5 for details of the tomography procedure.

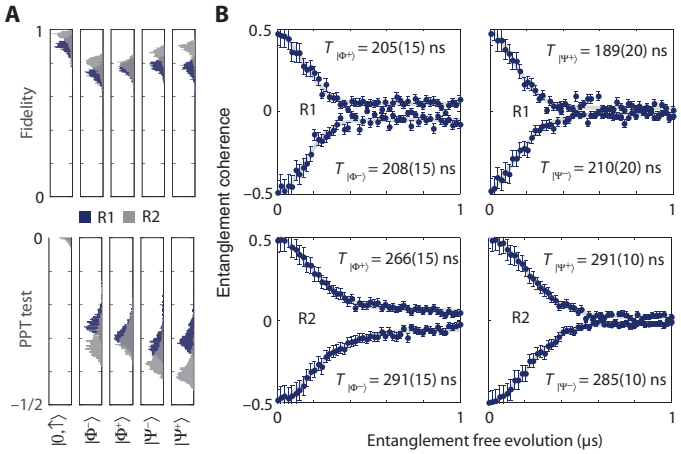

Fig. 4. Entanglement metrics. (**A**) The fidelity (upper panel) and the PPT test value (lower panel) as calculated from Monte Carlo and maximum likelihood techniques applied to the measured density matrices (see Materials and Methods for details). The lower labels show the ideal states. The initialized states are classical (PPT test ≥0), and the Bell states are unambiguously entangled (PPT test <0). (**B**) The entanglement coherences, $\langle -1, \uparrow|\rho|0, \downarrow\rangle$ for $|\Phi^{\pm}\rangle$ and $\langle -1, \downarrow|\rho|0, \uparrow\rangle$ for $|\Psi^{\pm}\rangle$, as a function of the entanglement free-evolution time. The error bars are 95% confidence intervals.

and final density matrices (see Fig. 3F for R2 data and fig. S3 for R1 data).

DISCUSSION

The density matrix after optical pumping shows strong initialization into $|0, \uparrow\rangle$ with fidelity (F) up to $0.95^{+0.05}_{-0.07}$. The density matrices after the entangling algorithm have F up to 0.88 ± 0.07 with respect to the ideal Bell states. To quantify the level of entanglement, we apply the Peres-Horodecki test (otherwise known as the "PPT" test; see Materials and Methods for details), which returns negative values for entangled states, with −0.5 signifying maximal entanglement. According to this metric, all of our reconstructed density matrices are unambiguously entangled, reaching a minimum PPT test value of −0.40 ± 0.06 (Fig. 4A). In the future, distillation protocols can be used to purify the entanglement (*37*). To measure the lifetimes of the Bell states, we allow them to freely evolve for a variable time before tomographically resolving their respective entanglement coherences ($\langle -1, \uparrow|\rho|0, \downarrow\rangle$ for $|\Phi^{\pm}\rangle$ and $\langle -1, \downarrow|\rho|0, \uparrow\rangle$ for $|\Psi^{\pm}\rangle$; see Fig. 4B). The lifetimes of these states could be extended via dynamical decoupling (*12*).

Entanglement in a spin ensemble at ambient conditions has reached a milestone in the study of macroscopic quantum systems. Register ensembles can be used for entanglement-enhanced sensors that use quantum error correction (*24*, *25*) or spin squeezing (*38*). They can serve as testbeds of cavity quantum electrodynamics at room temperature or can be used for long-lived quantum memory (*19*). The presented methods are equally applicable at cryogenic conditions, in which spin ensembles can couple collectively to other remote ensembles (*21*), to superconducting (*22*, *23*) and mechanical (*20*) resonators, and to optical fields (*18*). Exploiting these strong interactions is a promising route toward producing larger registers for quantum computing and metrology or distributing entanglement between remote nodes for quantum communication.

MATERIALS AND METHODS

Register Hamiltonian

The ground-state spin Hamiltonian of an R1 or R2 register is

$$H = \gamma_e \mathbf{S}\cdot\mathbf{B} - \gamma_n \mathbf{I}\cdot\mathbf{B} + \mathbf{S}\cdot\mathbf{A}\cdot\mathbf{I} + D_{ZFS}S_z^2 \quad (3)$$

where **S** is the vector of electronic $S = 1$ spin matrices, **I** is the vector of nuclear $I = ½$ spin matrices, $\gamma_n = -8.5$ MHz/T is the ^{29}Si nuclear gyromagnetic ratio, γ_e is the electronic gyromagnetic ratio, $D_{ZFS} = 1.352$ GHz is the PL6 electronic spin zero field splitting, **A** is the hyperfine coupling tensor, and **B** is the external magnetic field vector. The first term of Eq. 3 is the electronic Zeeman effect, the second term is the nuclear Zeeman effect, the third term is the electron-nuclear hyperfine interaction, and the fourth term is the electronic zero field spin splitting.

To confirm that the nuclei in R1 and R2 are ^{29}Si, and to extract their hyperfine coupling constants, we measured ODNMR as a function of the magnetic field $B_{||}$ (Fig. 2D, inset). To obtain a model for the ODNMR resonance frequencies, we diagonalized the Hamiltonian given in Eq. 3, approximating the hyperfine interaction to be isotropic ($\mathbf{A} = A\mathbf{I}$), which is justified by our discussion in section S4 and previous reports (*16*, *17*). We found that the ODNMR resonance frequencies in the electronic $m_S = -1$ spin manifold before and after $\left(f_{\lessgtr}\right)$ the ground-state spin level anticrossing ($B_{||} = 48.3$ mT for PL6) should follow the following relations

$$f_{\lessgtr} = \frac{1}{4}\left(3A + 2D_{ZFS} - 2B_{\|}(\gamma_e - \gamma_n)\mp \sqrt{8A^2 + \left(A - 2D_{ZFS} + 2B_{\|}(\gamma_e + \gamma_n)\right)^2}\right) \quad (4)$$

We fit our ODNMR data to these models, leaving A and γ_n as free parameters, and assumed that there is a negligible magnetic field misalignment. We found excellent fits for both R1 and R2, with best-fit parameters $A_{R1} = 12.62 \pm 0.08$ MHz, $A_{R2} = 9.59 \pm 0.03$ MHz, $\gamma_{n,R1} = -8.6 \pm 0.5$ MHz/T, and $\gamma_{n,R2} = -8.6 \pm 1.6$ MHz/T. The error bars are 95% confidence intervals. These values are consistent with a previous report in the literature (*16*), which determined these parameters using electron spin echo envelope modulation. From the extracted gyromagnetic ratios, we concluded that ^{29}Si is the nuclear spin in both R1 and R2. No ^{13}C-containing registers were characterized in this study.

Experimental methods

Our sample is an unprocessed chip of 4*H*-SiC from a stock wafer purchased from Cree Inc. (serial no. W4TRD0R-0200, BJ148-10). PL6 defects are present in the as-purchased material. The chip was positioned above a 0.5-mm-wide short-terminated stripline, which is used as an antenna for microwave and radio-frequency fields. The three microwave signals used for electron spin manipulation were generated by two Stanford Research (SG396) vector signal generators and an Agilent E8257C signal generator. The radio-frequency signal used for nuclear spin manipulation was digitally synthesized by an arbitrary waveform generator (Tektronix AWG 5014c). All signals were band-pass–filtered, gated with switches (MiniCircuits ZASWA-2-50DR+), multiplexed (MiniCircuits ZFSC-4-1-S+), and amplified (AR 30W1000B) before reaching the stripline antenna. We split off a small portion of the amplified signal at a −20-dB port of a directional coupler (Narda, model 4216-20) and passed it through a Schottky diode (Herotek, model DZM185AB) and then into an oscilloscope to monitor the microwave

pulses. A permanent magnet (K&J Magnetics Grade N52 magnet) provided the magnetic field $B_{||}$, which was along the PL6 quantization axis (the 4H-SiC *c* axis).

Registers were off-resonantly addressed through their phonon sideband with 975-nm light from a diode laser (ThorLabs, model PL980P330J). The laser was gated with an acousto-optic modulator (Gooch & Housego, model R21200-1DS). The excitation power was 100 mW at the back aperture of an infrared-optimized objective (Olympus, model LCPLN50XIR), and the excitation volume was about $\pi \times (1.5\ \mu m)^2 \times 6\ \mu m \sim 40\ \mu m^3$, where we have used our approximate laser spot size (3 μm in diameter) and depth of field (6 μm in length). Photoluminescence was collected through the same objective, isolated from the excitation beam with a dichroic mirror, filtered with a 980-nm long-pass filter (Semrock), and measured with an infrared-optimized photo-receiver (Electro Optical Components, model OE-200-IN). Registers near the periphery of the laser spot contributed to the signal, but the signal was dominated by registers near the center. The detector signal was preamplified (Stanford Research Systems, model SR560) and demodulated with a lock-in amplifier (PerkinElmer, model 7265). A schematic of our experimental apparatus is presented in fig. S4.

Frequency-selective, nonlocal, electronic gates were performed with Gaussian-shaped pulses. Inversion pulses (that is, spin rotations by π radians) had a full-width at half maximum that was typically 150 ns, with a corresponding bandwidth of 4.2 MHz. This bandwidth is wide enough to encompass the ~1.1-MHz electron spin transition linewidths while maintaining good frequency selectivity. The frequency-nonselective, local, electronic gates were implemented with rectangular pulses. Inversion pulses were of 20 ns width, with an approximate 45-MHz bandwidth. Frequency-selective, nonlocal, nuclear gates were performed with rectangular pulses. Inversion pulses lasted 6000 ns, with an approximate bandwidth of 150 kHz, which is enough to fully encompass their ~10-kHz inhomogeneously broadened nuclear spin transition linewidths. In the entangling algorithm, we applied a three-gate composite pulse to drive the initial electronic inversion $|0, \uparrow\rangle \rightarrow |-1, \uparrow\rangle$. By choosing the phases of our gates, we can implement spin rotations about different axes. For register initialization and readout, we used a 50-μs-long laser pulse. This pulse length saturates the initialization process, which, as we have measured, takes 729 ± 350 ns for the electrons and $2.2^{+3.5}_{-2.2}$ μs for the nuclei (95% confidence intervals are given).

For the ODMR measurement presented in Fig. 2A, we locked into the microwave pulse being on versus off. The ODMR signal (Fig. 2B), which we quoted in arbitrary units, is related to the population that was transferred from $m_S = 0$ to $m_S = -1$. For the ODNMR measurement presented in Fig. 2C, the microwave pulse frequency was chosen to be broadband, such that it excited the $|0, \uparrow\rangle \rightarrow |-1, \uparrow\rangle$ transition of R1 and R2 simultaneously. For this measurement, we locked into the radio-frequency pulse being on versus off. The ODNMR signal (Fig. 2D), which we quoted in arbitrary units, is related to the population that was transferred from $m_I = \uparrow$ to $m_I = \downarrow$. We note that a strong ODNMR signal near the R1 and R2 hyperfine splitting is observed only when the first MW pulse is applied. This observation implies that the PL6 optical cycle preferentially polarizes its electron into $m_S = 0$, where the hyperfine interaction is absent, and not into $m_S = \pm 1$. Similar arguments have previously been made to determine the state of polarization of nitrogen-vacancy color centers in diamond (*8*).

Most measurements presented here were performed at $B_{||} = 33$ mT. At this magnetic field, R1 and R2 are both at their hyperfine-mediated, excited-state level anticrossings (*15*, *16*). Near its excited-state level anticrossing, a register's electron and nuclear spins are hybridized (the $|0, \downarrow\rangle$ and $|-1, \uparrow\rangle$ states in particular), enabling them to exchange polarization after optical pumping. In addition to driving dynamic nuclear polarization (*16*, *17*), this polarization exchange leads the R1 and R2 photoluminescence intensities to be nuclear spin–dependent [previously observed in nitrogen-vacancy centers in diamond (*10*)]. For this reason, at $B_{||} = 33$ mT, each register's nuclear spin can be read out directly, without needing to first project it onto its coupled electron spin. Far from $B_{||} = 33$ mT, however, R1 and R2 are no longer at their excited-state level anticrossings, and thus their nuclear spins are no longer hybridized with their coupled electron spins. At those magnetic fields, each register's nuclear spin must be projected onto its electron spin for readout, which can be accomplished with a $C_{\uparrow}ROT_e$ gate. This gate was used for the spectroscopic measurements in the inset to Fig. 2D. We did not apply this gate in our ODNMR-based tomography protocol to minimize crosstalk and pulse errors.

Entanglement metrics

To compute the fidelity *F* of a density matrix ρ with respect to another density matrix ρ′, we used the definition (*39*)

$$F = \mathrm{Tr}\left(\sqrt{\sqrt{\rho}\rho'\sqrt{\rho}}\right)^2 \quad (5)$$

To compute the PPT test value (*40*, *41*) of ρ, we found the minimum eigenvalue of ρ^{T_n}. T_n is the partial transpose which can be taken over either by the electron or the nuclear spin subspace.

To compute these values from our measured data, we took the following approach: First, we applied a Monte Carlo algorithm to determine the distribution of possible electron spin polarizations from our data (see section S2 for details). We then sampled this distribution 10^3 times and combined it with the tomographic measurements discussed in the main text to produce 10^3 corresponding density matrices. We then added a random, normally distributed error to each element of each density matrix, which was commensurate with that element's measurement uncertainty, and then located the most likely physical density matrix via maximum likelihood estimation (*42*). For each of the resulting physical density matrices, we computed *F* and the PPT test values, as defined above, which resulted in the distributions plotted in Fig. 4A. In the main text, we quoted the means and 95% confidence intervals of these approximately normal distributions. These data are consolidated in table S4.

SUPPLEMENTARY MATERIALS

Supplementary material for this article is available at http://advances.sciencemag.org/cgi/content/full/1/10/e1501015/DC1

Section S1. Multinuclear spin registers.
Section S2. Electron spin polarization.
Section S3. Register-density calculation.
Section S4. Coherent nuclear spin control.
Section S5. Quantum-state tomography.
Fig. S1. Optically pumped electron spin polarization.
Fig. S2. Coherent nuclear spin control in SiC.
Fig. S3. Entanglement of the R1 ensemble.
Fig. S4. Experimental apparatus.
Table S1. The relative signal calculated for various registers.
Table S2. Quantum gate sequences used to measure the density matrix coherences.
Table S3. Quantum gate sequences used to measure the density matrix populations.
Table S4. Consolidated initialization and entanglement data.
References (*43*–*48*)

REFERENCES AND NOTES

1. D. G. Cory, A. F. Fahmy, T. F. Havel, Ensemble quantum computing by NMR spectroscopy. *Proc. Natl. Acad. Sci. U.S.A.* **94**, 1634–1639 (1997).
2. N. A. Gershenfeld, I. L. Chuang, Bulk spin-resonance quantum computation. *Science* **275**, 350–356 (1997).
3. M. S. Anwar, D. Blazina, H. A. Carteret, S. B. Duckett, T. K. Halstead, J. A. Jones, C. M. Kozak, R. J. K. Taylor, Preparing high purity initial states for nuclear magnetic resonance quantum computing. *Phys. Rev. Lett.* **93**, 040501 (2004).
4. D. Deutsch, Quantum theory, the Church-Turing principle and the universal quantum computer. *Philos. Trans. R. Soc. A* **400**, 97–117 (1985).
5. E. Knill, I. Chuang, R. Laflamme, Effective pure states for bulk quantum computation. *Phys. Rev. A* **57**, 3348–3363 (1998).
6. S. L. Braunstein, C. M. Caves, R. Jozsa, N. Linden, S. Popescu, R. Schack, Separability of very noisy mixed states and implications for NMR quantum computing. *Phys. Rev. Lett.* **83**, 1054–1057 (1999).
7. S. Simmons, R. M. Brown, H. Riemann, N. V. Abrosimov, P. Becker, H.-J. Pohl, M. L. W. Thewalt, K. M. Itoh, J. J. L. Morton, Entanglement in a solid-state spin ensemble. *Nature* **470**, 69–72 (2011).
8. F. Jelezko, T. Gaebel, I. Popa, M. Domhan, A. Gruber, J. Wrachtrup, Observation of a coherent oscillation of a single nuclear spin and realization of a two-qubit conditional quantum gate. *Phys. Rev. Lett.* **93**, 130501 (2004).
9. V. Jacques, P. Neumann, J. Beck, M. Markham, D. Twitchen, J. Meijer, F. Kaiser, G. Balasubramanian, F. Jelezko, J. Wrachtrup, Dynamic polarization of single nuclear spins by optical pumping of nitrogen-vacancy color centers in diamond at room temperature. *Phys. Rev. Lett.* **102**, 057403 (2009).
10. M. Steiner, P. Neumann, J. Beck, F. Jelezko, J. Wrachtrup, Universal enhancement of the optical readout fidelity of single electron spins at nitrogen-vacancy centers in diamond. *Phys. Rev. B* **81**, 035205 (2010).
11. P. Neumann, N. Mizouchi, F. Rempp, P. Hemmer, H. Watanabe, S. Yamasaki, V. Jacques, T. Gaebel, F. Jelezko, J. Wrachtrup, Multipartite entanglement among single spins in diamond. *Science* **320**, 1326–1329 (2008).
12. T. van der Sar, Z. H. Wang, M. S. Blok, H. Bernien, T. H. Taminiau, D. M. Toyli, D. A. Lidar, D. D. Awschalom, R. Hanson, V. V. Dobrovitski, Decoherence-protected quantum gates for a hybrid solid-state spin register. *Nature* **484**, 82–86 (2012).
13. W. Pfaff, T. H. Taminiau, L. Robledo, H. Bernien, M. Markham, D. J. Twitchen, R. Hanson, Demonstration of entanglement-by-measurement of solid-state qubits. *Nat. Phys.* **9**, 29–33 (2013).
14. F. Dolde, V. Bergholm, Y. Wang, I. Jakobi, B. Naydenov, S. Pezzagna, J. Meijer, F. Jelezko, P. Neumann, T. Schulte-Herbrüggen, J. Biamonte, J. Wrachtrup, High-fidelity spin entanglement using optimal control. *Nat. Commun.* **5**, 3371 (2014).
15. G. Waldherr, Y. Wang, S. Zaiser, M. Jamali, T. Schulte-Herbrüggen, H. Abe, T. Ohshima, J. Isoya, J. F. Du, P. Neumann, J. Wrachtrup, Quantum error correction in a solid-state hybrid spin register. *Nature* **506**, 204–207 (2014).
16. A. L. Falk, P. V. Klimov, V. Ivády, K. Szász, D. J. Christle, W. F. Koehl, Á Gali, D. D. Awchalom, Optical polarization of nuclear spins in silicon carbide. *Phys. Rev. Lett.* **114**, 247603 (2015).
17. V. Ivády, K. Szász, A. L. Falk, P. V. Klimov, D. J. Christle, E. Janzén, I. A. Abrikosov, D. D. Awschalom, A. Gali, Theoretical model of dynamic spin polarization of nuclei coupled to paramagnetic point defects in diamond and silicon carbide. *Phys. Rev. B* **92**, 115206 (2015).
18. L.-M. Duan, M. D. Lukin, J. I. Cirac, P. Zoller, Long-distance quantum communication with atomic ensembles and linear optics. *Nature* **414**, 413–418 (2001).
19. E. Abe, H. Wu, A. Ardavan, J. J. L. Morton, Electron spin ensemble strongly coupled to a three-dimensional microwave cavity. *Appl. Phys. Lett.* **98**, 251108 (2011).
20. Y. Chang, C. P. Sun, Analog of the electromagnetically-induced-transparency effect for two nanomechanical or micromechanical resonators coupled to a spin ensemble. *Phys. Rev. A* **83**, 053834 (2011).
21. H. Weimer, N. Y. Yao, M. D. Lukin, Collectively enhanced interactions in solid-state spin qubits. *Phys. Rev. Lett.* **110**, 067601 (2013).
22. D. I. Schuster, A. P. Sears, E. Ginossar, L. DiCarlo, L. Frunzio, J. J. L. Morton, H. Wu, G. A. D. Briggs, B. B. Buckley, D. D. Awschalom, R. J. Schoelkopf, High-cooperativity coupling of electron-spin ensembles to superconducting circuits. *Phys. Rev. Lett.* **105**, 140501 (2010).
23. Y. Kubo, F. R. Ong, P. Bertet, D. Vion, V. Jacques, D. Zheng, A. Dréau, J.-F. Roch, A. Auffeves, F. Jelezko, J. Wrachtrup, M. F. Barthe, P. Bergonzo, D. Esteve, Strong coupling of a spin ensemble to a superconducting resonator. *Phys. Rev. Lett.* **105**, 140502 (2010).
24. G. Arrad, Y. Vinkler, D. Aharonov, A. Retzker, Increasing sensing resolution with error correction. *Phys. Rev. Lett.* **112**, 150801 (2014).
25. E. M. Kessler, I. Lovchinsky, A. O. Sushkov, M. D. Lukin, Quantum error correction for metrology. *Phys. Rev. Lett.* **112**, 150802 (2014).
26. P. G. Baranov, I. V. Il'in, E. N. Mokhov, M. V. Muzafarova, S. B. Orlinskii, J. Schmidt, EPR identification of the triplet ground state and photoinduced population inversion for a Si-C divacancy in silicon carbide. *J. Exp. Theor. Phys. Lett.* **82**, 441–443 (2005).
27. N. T. Son, P. Carlsson, J. ul Hassan, E. Janzén, T. Umeda, J. Isoya, A. Gali, M. Bockstedte, N. Morishita, T. Ohshima, H. Itoh, Divacancy in 4H-SiC. *Phys. Rev. Lett.* **96**, 055501 (2006).
28. W. F. Koehl, B. B. Buckley, F. J. Heremans, G. Calusine, D. D. Awschalom, Room temperature coherent control of defect spin qubits in silicon carbide. *Nature* **479**, 84–87 (2011).
29. V. A. Soltamov, A. A. Soltamova, P. G. Baranov, I. I. Proskuryakov, Room temperature coherent spin alignment of silicon vacancies in 4*H*- and 6*H*-SiC. *Phys. Rev. Lett.* **108**, 226402 (2012).
30. A. L. Falk, B. B. Buckley, G. Calusine, W. F. Koehl, V. V. Dobroviski, A. Politi, C. A. Zorman, P. X.-L. Feng, D. D. Awschalom, Polytype control of spin qubits in silicon carbide. *Nat. Commun.* **4**, 1819 (2013).
31. H. Kraus, V. A. Soltamov, D. Riedel, S. Väth, F. Fuchs, A. Sperlich, P. G. Baranov, V. Dyakanov, G. V. Astakhov, Room temperature quantum microwave emitters based on spin defects in silicon carbide. *Nat. Phys.* **10**, 157 (2014).
32. P. V. Klimov, A. L. Falk, B. B. Buckley, D. D. Awschalom, Electrically driven spin resonance in silicon carbide color centers. *Phys. Rev. Lett.* **112**, 087601 (2014).
33. A. L. Falk, P. V. Klimov, B. B. Buckley, V. Ivády, I. A. Abrikosov, G. Calusine, W. F. Koehl, A. Gali, D. D. Awschalom, Electrically and mechanically tunable electron spins in silicon carbide color centers. *Phys. Rev. Lett.* **112**, 187601 (2014).
34. D. J. Christle, A. L. Falk, P. Andrich, P. V. Klimov, J. Ul Hassan, N. T. Son, E. Janzén, T. Ohshima, D. D. Awschalom, Isolated electron spins in silicon carbide with millisecond coherence times. *Nat. Mater.* **14**, 160–163 (2015).
35. M. Widmann, S.-Y. Lee, T. Rendler, N. T. Son, H. Fedder, S. Paik, L.-P. Yang, N. Zhao, S. Yang, I. Booker, A. Denisenko, M. Jamali, S. A. Momenzadeh, I. Gerhardt, T. Ohshima, A. Gali, E. Janzén, J. Wrachtrup, Coherent control of single spins in silicon carbide at room temperature. *Nat. Mater.* **14**, 164–168 (2015).
36. L. Robledo, H. Bernien, T. van der Sar, R. Hanson, Spin dynamics in the optical cycle of single nitrogen-vacancy centres in diamond. *New J. Phys.* **13**, 025013 (2011).
37. C. H. Bennett, H. J. Bernstein, S. Popescu, B. Schumacher, Concentrating partial entanglement by local operations. *Phys. Rev. A* **53**, 2046 (1996).
38. T. Fernholz, H. Krauter, K. Jensen, J. F. Sherson, A. S. Sørensen, E. S. Polzik, Spin squeezing of atomic ensembles via nuclear-electronic spin entanglement. *Phys. Rev. Lett.* **101**, 073601 (2008).
39. M. A. Nielsen, I. L. Chuang, *Quantum Computation and Quantum Information*, chap. 9 (Cambridge Univ. Press, New York, 2010).
40. M. Horodecki, P. Horodecki, R. Horodecki, Separability of mixed states: Necessary and sufficient conditions. *Phys. Lett. A* **223**, 1–8 (1996).
41. A. Peres, Separability criterion for density matrices. *Phys. Rev. Lett.* **77**, 1413–1415 (1996).
42. K. Banaszek, G. M. D'Ariano, M. G. A. Paris, M. F. Sacchi, Maximum-likelihood estimation of the density matrix. *Phys. Rev. A* **61**, 010304 (1999).
43. N. B. Manson, J. P. Harrison, M. J. Sellars, Nitrogen-vacancy center in diamond: Model of the electronic structure and associated dynamics. *Phys. Rev. B* **74**, 104303 (2006).
44. D. M. Toyli, D. J. Christle, A. Alkauskas, B. B. Buckley, C. G. Van de Walle, D. D. Awschalom, Measurement and control of single nitrogen-vacancy center spins above 600 K. *Phys. Rev. X* **2** 031001 (2012).
45. J. Harrison, M. J. Sellars, N. B. Manson, Measurement of the optically induced spin polarization of N-V centres in diamond. *Diamond Relat. Mater.* **15**, 586–588 (2006).
46. R. I. Shrager, R. W. Hendler, Some pitfalls in curve-fitting and how to avoid them: A case in point. *J. Biochem. Biophys. Methods* **36**, 157–173 (1998).
47. E. Laloy, J. A. Vrugt, High-dimensional posterior exploration of hydrologic models using multiple-try $\text{DREAM}_{(ZS)}$ and high-performance computing. *Water Resour. Res.* **48**, W01526 (2012).
48. N. T. Son, T. Umeda, J. Isoya, A. Gali, M. Bockstedte, B. Magnusson, A. Ellison, N. Morishita, T. Ohshima, H. Itoh, E. Janzén, Divacancy model for P6/P7 centers in 4H- and 6H-SiC. *Mater. Sci. Forum* **527–529**, 527–530 (2006).

Acknowledgments: We thank C. De Las Casas, C. Anderson, W. F. Koehl, and Á. Gali for useful discussions. **Funding:** This work was supported by the Air Force Office of Scientific Research, the NSF DMR-1306300, and the NSF Materials Research Science and Engineering Centers. The work at the Ames Laboratory was supported by the Department of Energy–Basic Energy Sciences under contract no. DE-AC02-07CH11358. **Author contributions:** P.V.K., A.L.F., and D.J.C. performed the experiments. V.V.D. helped with the theory. D.D.A. supervised the efforts. All authors contributed to discussions, data analysis, and production of the manuscript. **Competing interests:** The authors declare that they have no competing interests. **Data and materials availability:** All data needed to evaluate the conclusions in the paper are present in the paper and/or the Supplementary Materials. Additional data related to this paper may be requested from the authors.

Submitted 30 July 2015
Accepted 14 October 2015
Published 20 November 2015
10.1126/sciadv.1501015

Citation: P. V. Klimov, A. L. Falk, D. J. Christle, V. V. Dobrovitski, D. D. Awschalom, Quantum entanglement at ambient conditions in a macroscopic solid-state spin ensemble. *Sci. Adv.* **1**, e1501015 (2015).

Science Advances

Quantum entanglement at ambient conditions in a macroscopic solid-state spin ensemble

Paul V. Klimov, Abram L. Falk, David J. Christle, Viatcheslav V. Dobrovitski and David D. Awschalom

Sci Adv **1** (10), e1501015.
DOI: 10.1126/sciadv.1501015